



Universiteit
Leiden
The Netherlands

Phase-separated lipid-based nanoparticles: selective behavior at the nano-bio interface

Papadopoulou, P.; Pol, R. van der; Hilten, N. van; Os, W.L. van; Pattipeiluhu, R.; Arias Alpizar, G.; ... ; Kros, A.

Citation

Papadopoulou, P., Pol, R. van der, Hilten, N. van, Os, W. L. van, Pattipeiluhu, R., Arias Alpizar, G., ... Kros, A. (2023). Phase-separated lipid-based nanoparticles: selective behavior at the nano-bio interface. *Advanced Materials*, 36(6).
doi:10.1002/adma.202310872

Version: Publisher's Version

License: [Creative Commons CC BY 4.0 license](https://creativecommons.org/licenses/by/4.0/)

Downloaded from: <https://hdl.handle.net/1887/3714178>

Note: To cite this publication please use the final published version (if applicable).

Phase-Separated Lipid-Based Nanoparticles: Selective Behavior at the Nano-Bio Interface

Panagiota Papadopoulou, Rianne van der Pol, Niek van Hilten, Winant L. van Os, Roy Pattipeiluhu, Gabriela Arias-Alpizar, Renzo Aron Knol, Willem Noteborn, Mohammad-Amin Moradi, Maria Joao Ferraz, Johannes Maria Franciscus Gerardus Aerts, Nico Sommerdijk, Frederick Campbell, Herre Jelger Risselada, Geert Jan Agur Sevink, and Alexander Kros*

The membrane-protein interface on lipid-based nanoparticles influences their *in vivo* behavior. Better understanding may evolve current drug delivery methods toward effective targeted nanomedicine. Previously, the cell-selective accumulation of a liposome formulation *in vivo* is demonstrated, through the recognition of lipid phase-separation by triglyceride lipases. This exemplified how liposome morphology and composition can determine nanoparticle-protein interactions. Here, the lipase-induced compositional and morphological changes of phase-separated liposomes—which bear a lipid droplet in their bilayer—are investigated, and the mechanism upon which lipases recognize and bind to the particles is unravelled. The selective lipolytic degradation of the phase-separated lipid droplet is observed, while nanoparticle integrity remains intact. Next, the Tryptophan-rich loop of the lipase is identified as the region with which the enzymes bind to the particles. This preferential binding is due to lipid packing defects induced on the liposome surface by phase separation. In parallel, the existing knowledge that phase separation leads to *in vivo* selectivity, is utilized to generate phase-separated mRNA-LNPs that target cell-subsets in zebrafish embryos, with subsequent mRNA delivery and protein expression. Together, these findings can expand the current knowledge on selective nanoparticle-protein communications and *in vivo* behavior, aspects that will assist to gain control of lipid-based nanoparticles.

1. Introduction

Lipid-based nanomedicine is a research field of growing importance, with various liposomal drug formulations marketed and used in the clinic over the last decades.^[1] More recently, lipid nanoparticles (LNPs) have been in the spotlight after their success in the mRNA vaccines against SARS-Cov-2, which was an important milestone for mRNA therapeutics paving the way for future innovations.^[2–6] Existing challenges in nanomedicine development however, including translational gaps, rapid clearance of nanoparticles from the systemic circulation, and the difficulty of targeting tissues beyond the liver, can hamper their clinical applicability.^[7,8] To push this technology forward, toward simpler, yet more efficient and tissue specific formulations for drug delivery, better understanding of nanoparticle behavior must be acquired, i.e., how lipid organization determines morphology and influences (desired) nano-bio interactions. A key step is to study the interactions of lipid-based nanoparticles with

P. Papadopoulou, R. van der Pol, N. van Hilten, W. L. van Os, R. Pattipeiluhu, G. Arias-Alpizar, R. A. Knol, F. Campbell, H. J. Risselada, A. Kros
Department of Supramolecular & Biomaterials Chemistry
Leiden Institute of Chemistry (LIC)
Leiden University
P. O. Box 9502, Leiden 2300 RA, The Netherlands
E-mail: a.kros@chem.leidenuniv.nl

W. Noteborn
NeCEN
Leiden University
Einsteinweg 55, Leiden 2333 AL, The Netherlands
M.-A. Moradi, N. Sommerdijk
Department of Chemical Engineering and Chemistry
Eindhoven University of Technology
P. O. Box 513, Eindhoven 5600 MB, The Netherlands

M. J. Ferraz, J. M. F. G. Aerts
Department of Medical Biochemistry
Leiden Institute of Chemistry (LIC)
Leiden University
P. O. Box 9502, Leiden 2300 RA, The Netherlands

N. Sommerdijk
Department of Medical BioSciences and Radboud Technology
Center – Electron Microscopy
Radboud University Medical Center
Nijmegen 6525 GA, The Netherlands

 The ORCID identification number(s) for the author(s) of this article can be found under <https://doi.org/10.1002/adma.202310872>

© 2023 The Authors. Advanced Materials published by Wiley-VCH GmbH. This is an open access article under the terms of the [Creative Commons Attribution](https://creativecommons.org/licenses/by/4.0/) License, which permits use, distribution and reproduction in any medium, provided the original work is properly cited.

DOI: 10.1002/adma.202310872

biologically relevant proteins, and how these are determined by lipid composition and morphology. Such interactions lead to the formation of a protein corona which controls the *in vivo* fate of nanoparticles to a great extent;^[9–12] or they induce morphological changes on the membrane and affect the supramolecular assembly,^[13,14] which in turn could also affect their *in vivo* fate.

Previously,^[15] in a liposome screening study in zebrafish embryos, a novel liposome formulation (named PAP3) was found to selectively interact with (capillary) lumen-bound triglyceride lipases (TGLs), enzymes involved in lipid transport and metabolism. The interaction led to the selective accumulation of PAP3 liposomes in brain endothelial cells (bECs) of zebrafish embryos which, at this developmental stage, are rich in TGLs. Liposome-lipase interactions were mediated solely through a unique phase-separated morphology, in which liposomes bare a single lipid droplet inside each bilayer (**Figure 1a**). This aspect was found to be the key element for the bEC-specific accumulation and interaction with TGLs.^[15] This is, to our knowledge, the first time that phase separation is used to target specific cells *in vivo*. PAP3 liposomes consist of an equimolar mixture of 1,2-distearyl-*sn*-glycero-3-phosphatidylcholine (DSPC)—a naturally occurring phospholipid—and 2-hydroxy-3-oleamidopropyl-oleate (DOaG), a synthetic lipid structurally analogous to a diacylglycerol (DAG) (**Figure 1a**). DAGs are endogenous signaling lipids and their conical shape, attributed to the small polar hydroxyl group and bulky fatty acid tails, is associated with negative curvature. When added to phospholipid membranes, they are known to perturb lamellar bilayers and induce phase separation and formation of nonbilayer phases (i.e., lipid droplets) above a threshold (miscibility) concentration.^[16,17] Endogenously, their local accumulation in the cell membrane induces morphological changes, which in turn potentiate recruitment and activation of proteins, e.g., Protein Kinase C (PKC) or Phospholipase C.^[18–20] DAGs have been also found to be main lipoprotein components, especially of high-density lipoproteins (HDLs).^[21,22] Our particular liposomal formulation follows similar principles and is a great example of how DAG analogues can generate lipid droplets within DSPC leaflets (i.e., lipid droplet is surrounded by a DSPC monolayer). Another important aspect of DAGs is that they increase the spacing between adjacent phospholipid headgroups in a lipid membrane, even below the threshold concentration, an effect that is amplified by curvature.^[23] The domains that form as a consequence of such packing frustrations and transiently expose the apolar domain of the lipid membrane, are known as lipid packing defects.^[17,24–26] Some membrane peripheral proteins have been proposed to rely on these hydrophobic lipid packing defects—caused by factors such as phase sep-

aration, lateral tension, or membrane curvature—for membrane binding and activation.^[27,28] Examples include the Golgi-associated protein ArfGAP1, that senses curvature-induced packing defects through an amphipathic lipid packing sensor motif^[29,30] and the CTP:phosphocholine cytidyltransferase (CCT), that binds to large packing defects on lipid droplets.^[31] Also, the toxin Equinatoxin-II^[32] and several lipases^[33,34] have been found to sense packing defects, induced by DAGs in particular.

TGLs are lipolytic enzymes bound at the luminal surface of capillaries, and are involved in lipid transport and metabolism, primarily through their interaction with freely circulating lipoproteins. They either hydrolyze tri- and diacylglycerols and cholesteryl esters residing in the lipoprotein core, remodeling lipoprotein particles and promoting influx of fatty acids into the cell; or they act as bridging molecules to facilitate lipoprotein cell uptake.^[35,36] The family consists mainly of hepatic lipase (HL),^[37] lipoprotein lipase (LPL),^[38] and endothelial lipase (EL).^[39] The main functional domains—the lipid binding domain for substrate binding, the lid region containing the catalytic triad of Serine (Ser), Aspartate (Asp), Histidine (His), and the heparin binding domain—are all structurally homologous throughout the lipase protein family (see refs. [40,41]; and **Figure S23** (Supporting Information) for protein alignment). The lipid binding domain is rich in hydrophobic residues, mainly tryptophans (Trp), forming a hydrophobic Trp-rich loop that is responsible for insertion of the protein in the hydrophobic lipid core of lipoproteins.^[37,42–45] Importantly, LPL has been found to depend on lipids on the lipoprotein membrane, but not apolipoproteins, for binding.^[46]

In this study, we elucidate the mechanism underpinning the selective interaction between PAP3 liposomes and TGLs, and observe selective morphological changes in the liposomes upon liposome-TGL incubation (**Figure 1b**). We combine experimental characterization and coarse-grained (CG) molecular dynamic (MD) simulations to investigate the molecular mechanism through which the TGL lipoprotein lipase interacts with the DOaG-rich phase-separated liposomes and observe any subsequent morphological changes of the liposomes upon incubation. By combining cryo-transmission electron microscopy (Cryo-TEM) with LPL enzymatic activity analysis, we observe selective lipolytic degradation of the lipid droplet of PAP3 liposomes (rich in DOaG), while the overall nanoparticle integrity and structure is maintained. Mass spectrometry analysis confirms the selective hydrolysis of DOaG over DSPC, consistent with the known preference of LPL for hydrolyzing tri- and diacylglycerols. Next, we built upon earlier insight in the role of defects for protein binding^[27,28] and study lipid packing defects in PAP3 liposomes and their role in recognition and binding of LPL. By combining Cryo-TEM with MD simulations we confirm and quantify increased packing defects on the curved DSPC monolayer surrounding the DOaG lipid droplet, leading to the insight that (induced) curvature and DOaG availability are the two likely ingredients for selective LPL binding. Free energy calculations and enzymatic activity analysis reveal that the Trp-rich loop of LPL acts as a lipid packing defect sensing motif, that prefers to interact with the defected PAP3 membrane (DSPC/DOaG), over the (flat) pure DSPC counterpart.

H. J. Risselada
Department of Physics
Technical University Dortmund
44221 Dortmund, Germany

G. J. A. Sevink
Department of Biophysical Organic Chemistry
Leiden Institute of Chemistry (LIC)
Leiden University
P. O. Box 9502, Leiden 2300 RA, The Netherlands

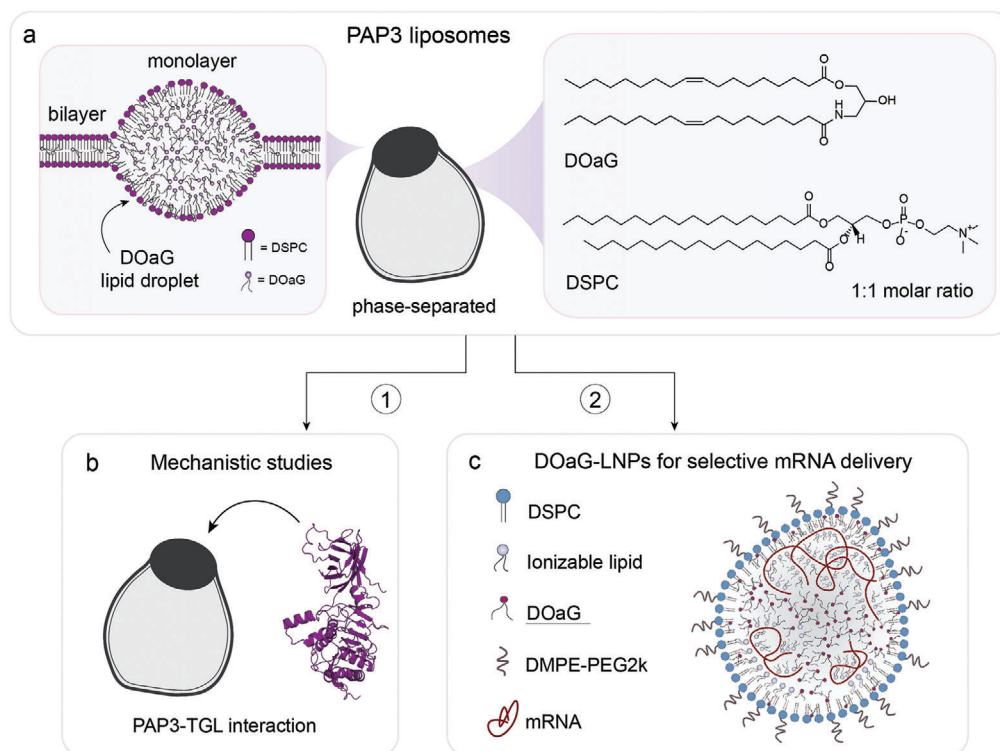


Figure 1. Molecular details of PAP3 liposomes and summary of current study. a) Schematic representation of phase-separated liposomes (named PAP3), molecular structures of DOaG and DSPC (1:1 ratio for liposome formation), and schematic explanation on how DOaG induces phase separation in DSPC membranes. PAP3 liposomes were further explored to b) elucidate the exact mechanism underpinning selective PAP3-TGL interactions and c) generate a novel DOaG-containing LNP formulation for selective mRNA delivery and expression. Schematic in (c) represents the hypothetical structure of an mRNA-LNP containing DOaG. TGL = triglyceride lipase.

Next, we investigate whether the DOaG lipid and the related phase separation is a novel, functional *in vivo* targeting modality that can be used to design a second-generation of lipid nanoparticle systems, providing cell-selective targeting and payload delivery (Figure 1c). Four mRNA-LNP formulations were created, and their morphology and *in vivo* behavior was assessed by cryo-TEM and in zebrafish embryos, respectively. Phase-separated mRNA-LNPs containing DOaG specifically accumulated in the BECs of zebrafish embryos, resulting in selective mRNA delivery and concomitant gene (protein) expression.

Overall, this study highlights that selective behavior at the nano-bio interface can be achieved by using membrane phase separation in lipid-based nanoparticles, as induced by the synthetic DAG analogue DOaG. Incorporated in liposomes and mRNA-LNPs, DOaG induces distinct lipid droplets, and hijacks an endogenous lipid transport and metabolism pathway leading to specific nanoparticle-protein communications and selective cell targeting.

2. Results

2.1. DOaG Lipid Droplet Selectively Depleted by Lipoprotein Lipase

As all TGLs hold high structural similarities and homology,^[40,41] LPL was chosen as the representative TGL due to the extensive

literature on its structure, regulation, and function. First, the phase-separated PAP3 liposomes were incubated with LPL and without LPL at physiological conditions for 3 h (pH 7.4, 37 °C), and Cryo-TEM imaging was used to assess any morphological changes on the liposomes (Figure 2a). As expected, without addition of LPL nearly 80% of PAP3 liposomes incubating at 37 °C for 3 h were phase-separated (Figure 2b–d; and Figure S1a, Supporting Information), with only ≈20% of the population having another morphology, i.e., either (multi-) lamellar, solid-lipid, or unidentifiable. Strikingly, when PAP3 liposomes were incubated with LPL, they were lacking the lipid droplet (Figure 2e; and Figure S1b, Supporting Information); less than 10% of the population appeared now to be phase-separated (Figure 2f,g) and almost 80% of the population were now lamellar. This indicated that LPL could deplete the phase-separated droplet possibly through its lipolytic activity, therefore selectively hydrolyzing the DOaG lipid. Accordingly, when the denatured and therefore inactive form of LPL was added to the PAP3 liposomes, no change of the phase-separated morphology or the percentage in the population was observed (Figure 2h–j; and Figure S1c, Supporting Information), implying the catalytically active LPL to be responsible for the selective droplet digestion. Interestingly, despite the major morphological change on PAP3 liposomes, the nanoparticles remained intact in terms of structural integrity, retaining their initial average hydrodynamic diameter of ≈120 nm over time, as determined by dynamic light scattering (DLS) (Figure S2 and Table S1, Supporting

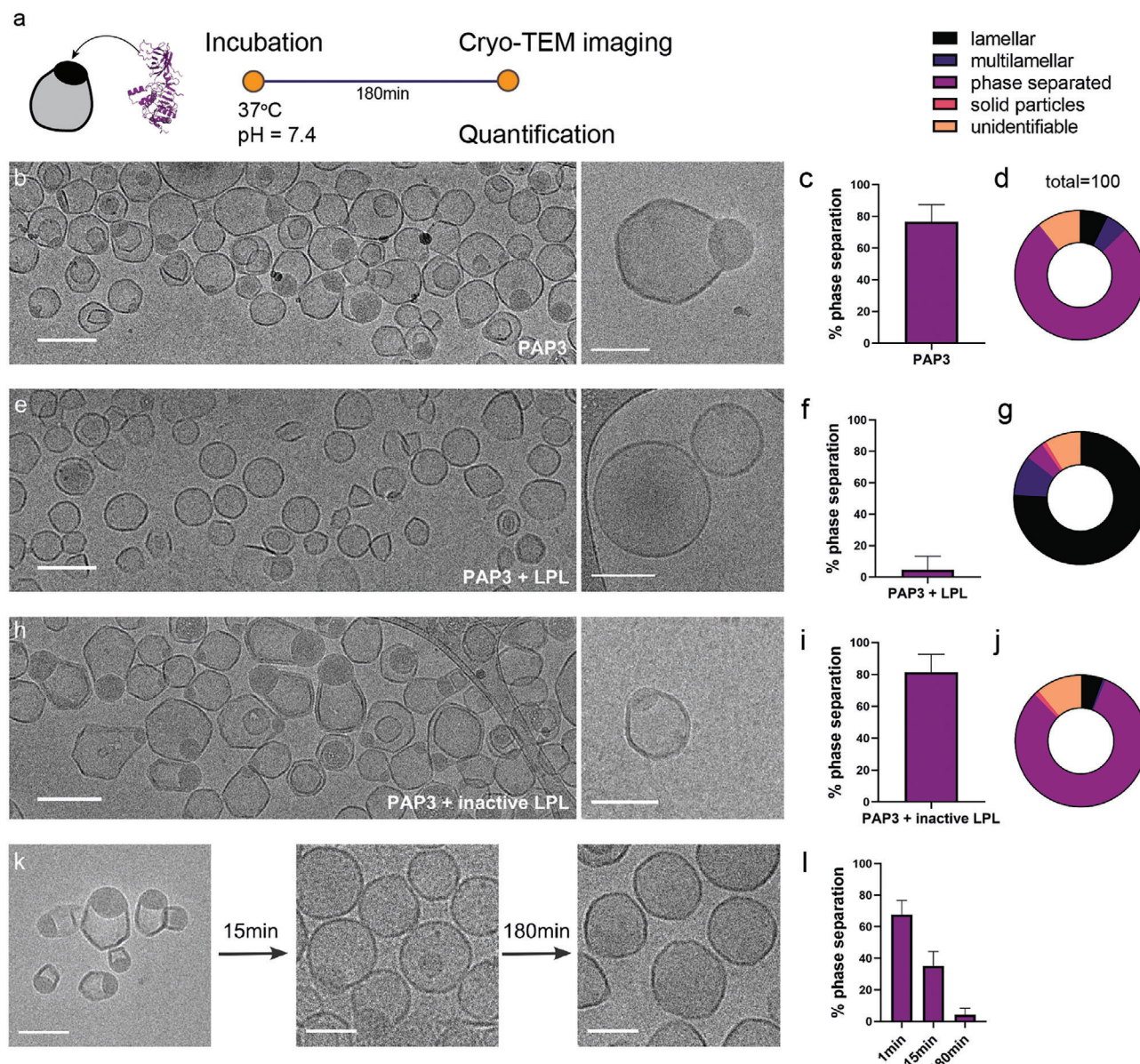


Figure 2. Selective depletion of DOaG lipid droplets in PAP3 liposomes. a) Schematic for conditions and timeline of cryo-TEM imaging. b) Low and high magnification cryo-TEM images depicting PAP3 liposomes at 37 °C incubating for 180 min. c) Percentage of phase separation on PAP3 liposomes based on cryo-TEM quantification ($N = 200$) and d) quantification of all populations found on PAP3 liposomal formulation incubating at 37 °C for 180 min. e) Low and high magnification cryo-TEM images depicting PAP3 liposomes incubating with LPL at 37 °C for 180 min. f) Percentage of phase separation on PAP3 liposomes based on cryo-TEM quantification ($N = 200$) and g) quantification of all populations found on the formulation after incubation with LPL at 37 °C for 180 min. h) Low and high magnification cryo-TEM images depicting PAP3 liposomes incubating with inactive LPL at 37 °C for 180 min. i) Percentage of phase separation on PAP3 liposomes based on cryo-TEM quantification ($N = 200$) and j) quantification of all populations found on the formulation after incubation with inactive LPL at 37 °C for 180 min. k) Cryo-TEM images of PAP3 liposomes incubating with LPL for 1, 15, and 180 min. l) Percentage of phase separation on PAP3 liposomes based on cryo-TEM quantification ($N = 200$) after incubation with LPL at 37 °C for 1, 15, and 180 min. The data set generated for this figure is a result of the same liposome formulation. Size and PDI values, as determined by DLS, can be found in Table S1 (Supporting Information). Scale bars: 200 nm for (b, e, h) and 100 nm for k and insets on (b, e, h).

Information). Of note, liposomes without DOaG (i.e., 100% DSPC), did not display any changes in morphology or size before and after addition of LPL (Figure S3 and Table S1, Supporting Information) suggesting no interaction and as before, signifying LPL to be selective for DOaG, or for the phase separation induced by DOaG.

2.2. LPL Selectively Hydrolyzes DOaG but Not DSPC

Subsequently, to assess the evolution and timeline of the observed morphological change, PAP3 liposomes were imaged after incubating with LPL for 1, 15, and 180 min, and the percentage of phase separation was found to progressively

decrease over time (Figure 2k,l; and Figure S4, Supporting Information). This indicated the observed phenomenon was a dynamic process, and that lipolysis could be monitored over time by quantifying the amount of free fatty acids (FFA),^[47,48] released as metabolite products from the hydrolysis of the co-formulants DOaG and/or DSPC (Figure S5a, Supporting Information). For this, a nonesterified free fatty acid measurement kit (NEFA-kit) was used, along with mass spectrometry which was used to determine which lipid is preferentially hydrolyzed (Figure S5b, Supporting Information). As expected, PAP3 liposomes incubated with LPL released ≈ 0.9 mmol L⁻¹ of FFA over a period of 300 min and hydrolysis continued beyond this point (Figure S5c, Supporting Information). Incubation of PAP3 liposomes without LPL, or incubation of PAP3 liposomes with inactivated LPL, as well as incubation of 100% DSPC liposomes with LPL, did not release any significant amount of FFA over the same period, again indicating the specificity of LPL for DOaG in mixed and/or phase-separated membranes (Figure S5c, Supporting Information). Here, to also verify the LPL preference on naturally occurring DAGs—along with DOaG as a DAG analogue—we formulated phase-separated liposomes consisting of dioleoylglycerol (DOG) and DSPC. Subsequently, we monitored the FFA release and structural changes of the DSPC/DOG liposomes upon LPL incubation (Figure S6, Supporting Information). The results showed similar preference of LPL on DOG-containing liposomes as on PAP3. Similarly, to assess the influence of LPL on liposomes that are known to freely circulate in vivo and not particularly interact with cells types and proteins,^[10,49] a formulation based on the clinically approved Myocet^[50] (composition: POPC:CHO_55:45) was also incubated at 37 °C with LPL for 180 min, which did not result in FFA release, indicating no interaction with LPL (Figure S7, Supporting Information). Next, mass spectrometry analysis was used to investigate the hydrolysis of the lipids in the PAP3 formulation. The DOaG/DSPC ratio was measured before and after addition of LPL, indicating a decrease only for the DOaG lipid after addition of LPL and signifying that 30.7% of DOaG was hydrolyzed (Figures S5d and S8, Supporting Information). Given that DOaG is the only lipid hydrolyzed, FFA was again measured immediately after the mass spectrometry and found to correspond to 31% of hydrolyzed DOaG, in agreement with the mass spectrometry value (Figure S5e, Supporting Information). In our previous studies,^[15] lipase-mediated uptake of PAP3 liposomes was inhibited in vivo (zebrafish embryos and adult mice) by the TGL inhibitor XEN445.^[51] Therefore, we investigated the influence of XEN445 on the lipolytic activity of LPL on PAP3. LPL was incubated with XEN445 at room temperature for 30 min, prior to the addition of LPL to PAP3 liposomes, and DOaG hydrolysis was found to be inhibited by $\approx 50\%$ at 500 μM XEN445 (Figures S5f and S9, Supporting Information).

2.3. Simulations Confirm Lipase Binds on PAP3 Liposomes Through Lipid Packing Defects and via Its Trp-Rich Lipoprotein Binding Domain

Having confirmed that LPL selectively hydrolyzes liposomes containing DOaG, we sought to investigate the role of the charac-

teristic phase-separated morphology. Previously, we showed that the concentration of DOaG lipid in the PAP3 formulation determines whether liposomes phase-separate. When PAP3 was formulated with DSPC and 0%, 10%, or 20% mol DOaG, liposomes did not show phase separation, while above 30% mol DOaG liposomes were found to be phase-separated, causing a directed in vivo biodistribution toward TGL rich endothelial cells.^[15] Therefore, we hypothesized phase separation to be essential, or at least preferable, for TGL recognition. To assess this hypothesis, released FFA after LPL incubation was measured for liposomes with varying % mol of DOaG. Up to 20% mol, i.e., for mixed membranes, FFA release increased linearly, but it steeply increased after this point (Figure 3a). This suggested enhanced LPL action for PAP3 liposomes with $\geq 30\%$ mol DOaG, which coincides with the concentration threshold relating to phase separation as quantified by Cryo-TEM (Figure 3a insets, Figure 3b right y-axis and Figure S10, Supporting Information). The finding that the phase change coincides with a nonlinear jump in the LPL-induced FFA release, signifies the role of phase separation in LPL hydrolysis.

As reported earlier for DAGs,^[16,17,20] increasing the DOaG content in a PC bilayer across a phase boundary, could substantially increase the membrane curvature in the surroundings of the lipid droplet. Curvature is known to notably increase the lipid packing defect number and area, an effect that has been suggested to promote protein binding.^[16,23,52] Moreover, compared to a mixed membrane, the local concentration of DOaG in the curved membrane around the lipid droplet is also significantly higher. Therefore, to quantify the role of phase separation, curvature, and packing defects at a molecular level—that is not directly accessible by experiments or atomistic MD due to long time scales—we generated a CG representation for DSPC/DOaG at different DOaG concentrations (snapshots in Figure 3b; and Figure S11a, Supporting Information). As detailed in Sections S12–S15 (Supporting Information), the CG DOaG lipid representation was adapted from the similar DOG lipid.^[53] In agreement with standard practice, we employed the observed phase separation onset at 29% mol (Figure 3b, left y-axis) to match the experimental findings. Phase separation in CGMD was quantified by the (time-averaged) relative fraction of contacts between the DOaG lipid and the DSPC lipid (see the Experimental Section for more details and Figure S14, Supporting Information) following a recently developed method.^[54] The DOaG parametrization described here was used for all simulations in the remainder of this study.

To capture the role of curvature and to quantify the defect characteristics for a DOaG droplet, embedded in a DSPC/DOaG monolayer, of a typical diameter of, i.e., an average of 22.3 nm for $\geq 30\%$ mol DOaG (see Figure 3c) as quantified by cryo-TEM—we performed a droplet simulation with this initial radius for a 82/18 DOaG/DSPC ratio (Figure 3d; and Figure S11b, Supporting Information). Since demixing is strongly diffusion limited, we started from a prestructured droplet and performed 2 microsecond of simulated annealing, to quickly reach a stable structure, with the droplet radius stabilizing to 20.1 nm. Using a modified protocol (see the Experimental Section), we calculated the packing defect constant, which is a measure of the effective average area of hydrophobic defects (Figure 3d,e; and Figure S16, Supporting Information). For a flat DSPC membrane the

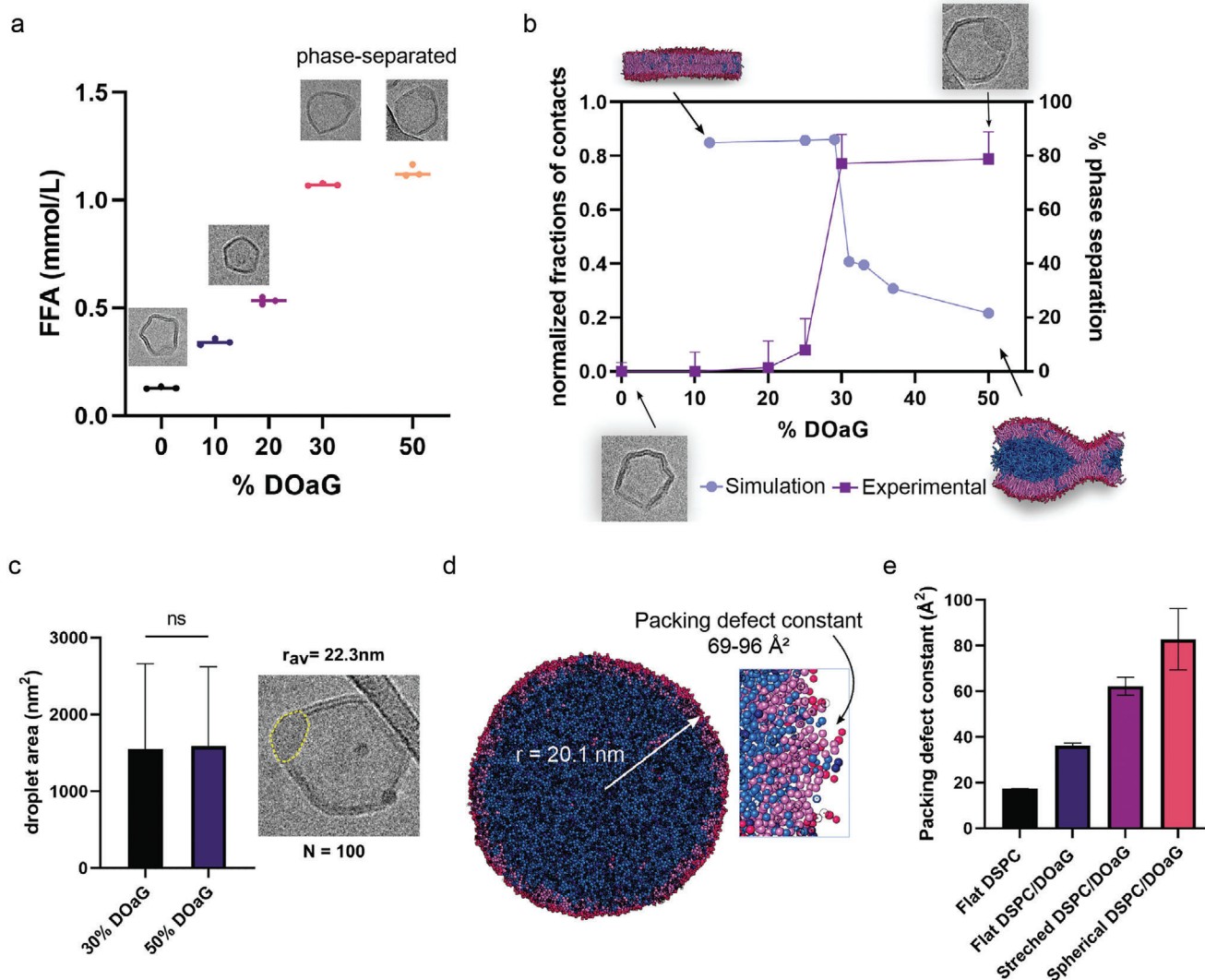


Figure 3. Experimental findings and simulations confirm phase separation as an important aspect for LPL preferential binding on PAP3 liposomes a) Quantification of released FFA of formulations containing DSPC and varying % mol of DOaG, after incubation with LPL at 37 °C for 120 min. Insets show the morphology of liposomes at a particular % mol DOaG (0% = gel phase, 20% = small droplet indicate initiation of phase separation, 30–50% = phase-separated). b) Double plot showing correlation of experimental and simulation data. Phase separation starts after 25% mol DOaG according to cryo-TEM quantification ($N = 200$) and 29% according to the coarse-grained simulation. DOaG is shown in blue and DSPC is shown in pink/red. Correlation of simulated PAP3 droplet and experimental values. c) Average radius of phase-separated PAP3 liposomes (containing 30% or 50% mol DOaG) as calculated by cryo-TEM quantification of the droplet area ($N = 100$). Area was measured in Fiji software, by drawing the perimetry of each droplet (yellow dashed line) according to the electron density. Experimental values were obtained to correlate the simulation data for the PAP3 model droplet. d) Simulated PAP3 droplet with radius approximately matching the experimental value and zoom-in inset depicting the lipid packing defects. Packing defect constant determined as the effective average area of hydrophobic defects and calculated to be 69–96 Å² for the spherical droplet. DOaG is shown in blue and DSPC is shown in pink/red. e) Packing defect constants of flat DSPC, flat DSPC/DOaG, stretched DSPC/DOaG, and spherical DSPC/DOaG (see d). Separate liposomal formulations were used to generate data in (a), (b), and (c). Size and PDI values, as determined by DLS, can be found in Table S1 (Supporting Information). Statistical significance was evaluated using a two-tailed unpaired Student's *t*-test. ns: not significant ($p > 0.05$). Significantly different: * $p \leq 0.05$, ** $p \leq 0.01$, *** $p < 0.001$. Exact *p* value for c: 0.8152, e: 0.0002, and <0.0001. For graphs in (b), lines were drawn for the clear visualization of the phase separation point.

constant was found to be $\approx 17 \text{ \AA}^2$ while adding the DOaG to the system (1:1 ratio) increased the constant to $\approx 36 \text{ \AA}^2$ indicating phase separation increases the packing defects. Also, adding curvature increased the packing defect constant even further—as calculated by the defect constant on the curved droplet (Figure 3d,e). For the latter, however, we give a range since the lipid composition in the droplet monolayer varies, depending

on the starting configuration and size, and because there is an uncertainty in the fitting parameter. The range for the packing defect constant was between 69 and 96 Å² showing that the packing defects in the curved droplet are more prevalent than in the flat pure DSPC and flat DSPC/DOaG membranes (Figure 3d zoom in, and Figure 3e). We next used the lower bound of this value range as a reference value for simulating LPL binding to

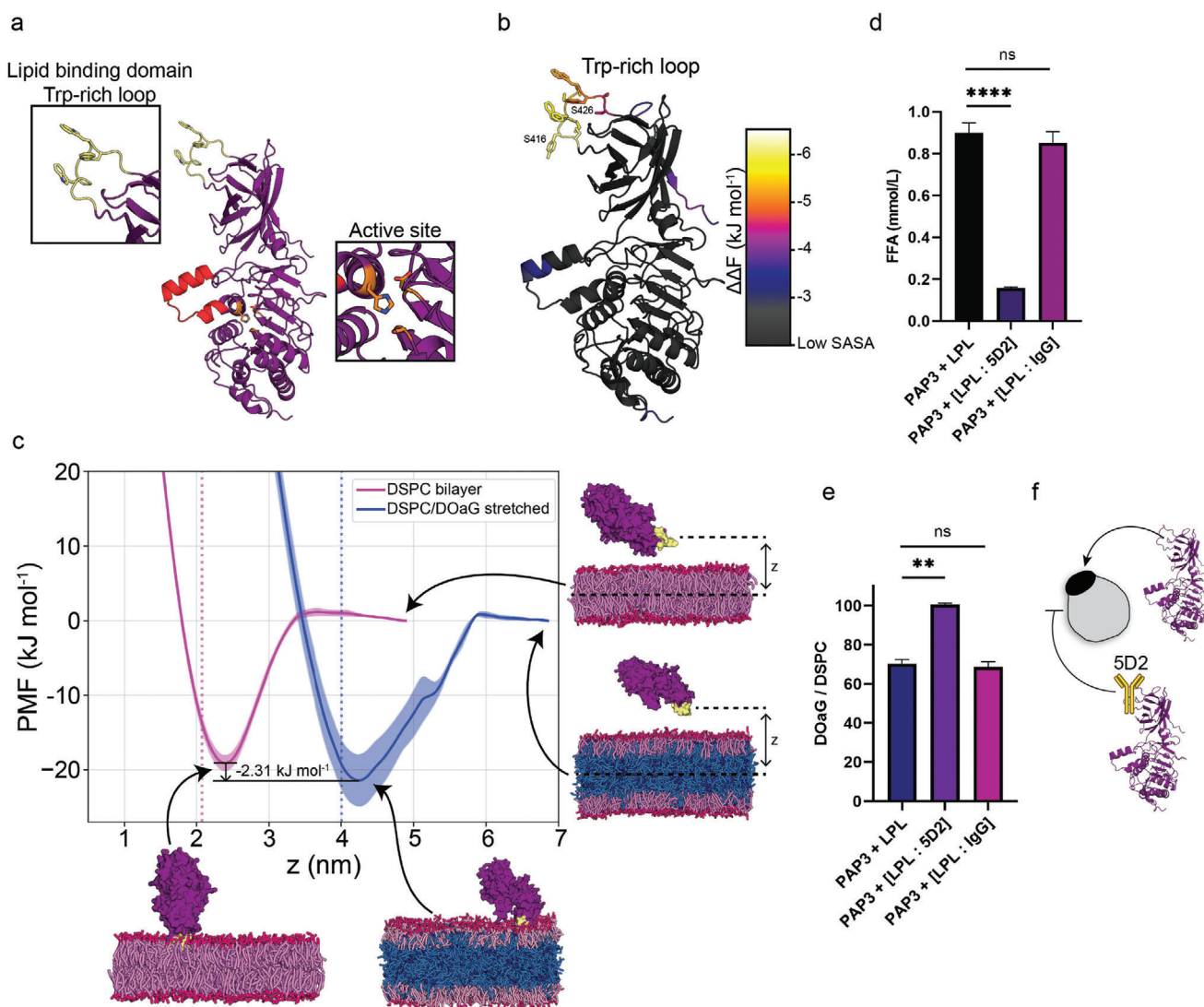


Figure 4. LPL binds to PAP3 liposomes via its Trp-loop. **a**) Structure of LPL (*Bos Taurus*). Insets indicate the Trp-rich loop (yellow)—which comprises the lipid binding domain—and active site (orange). Lid region indicated in red. **b**) Color-map of predicted lipid packing defect sensing regions on LPL (all values are given in Figure S19, Supporting Information). Bright colors indicate putative sensing motifs, according to NN-predicted relative $\Delta\Delta F$ and solvent-accessible surface area (SASA) values. **c**) PMF profiles of LPL binding to a DSPC membrane (in red-pink) and a DSPC/DOaG phase-separated membrane (in red-pink/blue). The US reaction coordinate is the z -distance between the center-of-mass (COM) of the Trp-rich loop (in yellow) and the COM of the lipids (i.e., center plane of the membrane). Snapshots are the final frames of the trajectories and indicate that the protein is completely unbound at high z (free energy = 0 kJ mol⁻¹) and membrane-bound through the Trp-rich loop at the minima. Dotted lines indicate the position of the DSPC head groups (NC3 beads). **d**) Quantification of released FFA from PAP3 liposomes after incubation at 37 °C for 120 min with LPL, LPL + 5D2 antibody, and LPL + IgG control antibody. **e**) Mass spectrometry quantification of DOaG/DSPC ratio of PAP3 liposomes incubating at 37 °C for 120 min with LPL, LPL + 5D2 antibody, and LPL + IgG control antibody. DOaG/DSPC ratio of liposomes that did not undergo hydrolysis incubating with LPL + 5D2 was set as 100. **f**) Schematic of LPL binding to PAP3 liposomes via its Trp-rich loop and 5D2 mediated inhibition of binding. The same liposomal formulation was used to generate data in (d) and (e). Size and PDI values, as determined by DLS, can be found in Table S1 (Supporting Information). Statistical significance was evaluated using a two-tailed unpaired Student's t -test. ns: not significant ($p > 0.05$). Significantly different: * $p \leq 0.05$, ** $p \leq 0.01$, *** $p < 0.001$. Exact p value for d: <0.0001 and 0.3222 and for e: 0.0029 and 0.5654.

stretched DOaG/DSPC membranes (Figure 3e and Figure 4c) (vide infra). Stretched membranes are used to approximate curved membranes, since the lipid packing defects on their outer leaflet surface correlate, as we explain in ref. [55].

Following the proof that the DOaG droplet increases both the number and area of lipid packing defects in the curved DSPC monolayer—due to the condensing of DOaG and the accompan-

ing high curvature of the outer leaflet—we next sought to investigate whether LPL specifically binds to PAP3 via these packing defects. The structure of LPL is well studied and identified by X-ray crystallography^[56] and Cryo-TEM^[57] (Figure 4a). Functional parts include the lipid binding domain which is rich in Trp as mentioned previously (hence called the Trp-rich loop, Figure 4a, inset), and the catalytic lid with the active site (Figure 4a, inset). The

C-terminus, where the lipoprotein binding domain is located, is responsible for substrate binding but not for heparin binding or catalysis.^[58] We first proceeded to investigate which regions of the LPL protein may be involved in interacting with the packing defects of the phase-separated membrane. Hereto, we employed a recently developed neural network (NN) model that is trained on MD data and is able to predict the lipid packing defect sensing free energy ($\Delta\Delta F$) for peptide sequences.^[59] $\Delta\Delta F$ is defined as the difference in free energy of a peptide binding to a tensionless membrane versus a stretched membrane that bares lipid packing defects, such as the curved DSPC monolayer around the DOaG lipid droplet. The higher the magnitude of the $\Delta\Delta F$ value, the more favorably it binds to the defected membrane. We first used a sliding window of 15 residues to fragmentize the LPL protein structure and then predicted the $\Delta\Delta F$ for the overlapping fragments. From this, we derived a per-residue average $\Delta\Delta F$ (given the residue is solvent accessible, see Section S17 and Figure S18, Supporting Information) and color-coded the protein structure accordingly (Figure 4b).

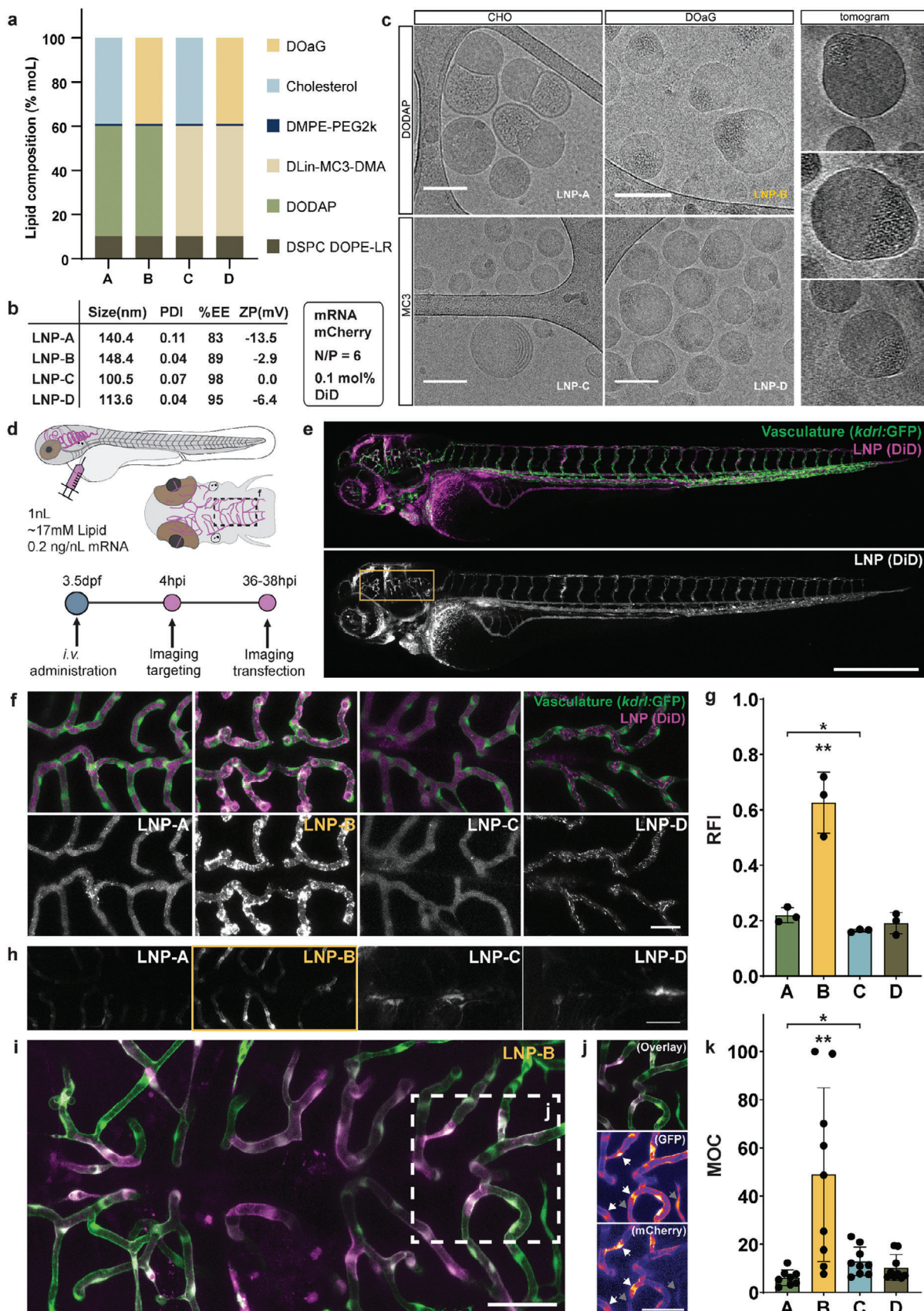
Residues Ser416-Ser426, comprising the Trp-rich loop, was the highest scoring solvent-accessible peptide motif, we identified (Figure 4b; and Section S19, Supporting Information). As previously described in the context of membrane curvature sensing, Trp residues can indeed play a key role in complementing the hydrophobic lipid packing defects on lipid leaflets,^[29] and we argue that the Trp-rich loop of LPL might fulfill a similar function. Notably, this argument is in line with the Trp-rich loop being part of the lipid binding domain of LPL, which is responsible for endogenous lipoprotein binding.^[42–44]

To further investigate lipid packing defect sensing by LPL and to see whether the Trp-loop is preferably binding to defected membranes, such as the PAP3 liposomes, we calculated the potential of mean force (PMF) profiles for the entire LPL protein binding to the PAP3 phase-separated membrane—with lipid packing defect constants that are in the same range as those for the earlier simulated PAP3 droplet (vide supra, Figure 3e). We performed umbrella sampling (US) simulations with the z-distance between the Trp-rich loop and the center plane of the membrane as the reaction coordinate. The resulting PMF profiles showed LPL binds to the PAP3 phase-separated membrane (having enhanced lipid packing defects) indeed more favorably than to a flat pure DSPC bilayer, with a small free energy difference of 2.31 kJ mol^{-1} ($\approx 1 k_B T$) between the minima (Figure 4c). The propensity for binding that is observed for the flat pure DSPC membrane (about 20 kJ mol^{-1}) corresponds exactly to the curvature sensing transition point from a recent study^[59] which showed that a 2 kJ mol^{-1} increase in binding free energy has a pronounced effect on the membrane binding probability (Figure S20, Supporting Information). Moreover, although a conformational change in the binding domain may contribute a few kJ mol^{-1} to the actual binding affinity,^[60] this shift is likely very similar for both membranes. Beyond this binding preference, the enzymatic preference of LPL to hydrolyze DAGs over phospholipids^[61] is not captured by our MD simulations but does contribute to our experimental observations. From the MD trajectories, it is clear that LPL indeed interacts with the membranes through its Trp-rich loop (snapshots in Figure 4c), in line with the NN-predictions (Figure 4b), and mechanistically similar to previously reported lipid droplet sensing proteins.^[62,63]

To experimentally assess the involvement of the Trp-rich loop in the recognition and hydrolysis of PAP3 liposomes, we measured the hydrolytic activity of LPL on PAP3 liposomes, while blocking the Trp-rich loop with the monoclonal anti-LPL antibody 5D2. The 5D2 monoclonal antibody has been identified to bind specifically to the Trp-loop of the lipid binding domain of LPL, inhibiting binding and catalysis of lipoproteins.^[44,64–66] Indeed, after incubation of LPL with 5D2 in a 1:1 ratio at room temperature for 30 min and subsequent addition to PAP3 liposomes, hydrolysis of DOaG as quantified by the release of FFA and mass spectrometry was strongly reduced (Figure 4d–f). To ensure that inhibition of hydrolysis was due to the specific inhibition of the Trp-rich loop by the 5D2 antibody, a negative isotype control antibody (matching 5D2 antibody's host species and class—IgG1) was used to measure the nonspecific binding in LPL and nonspecific interactions with PAP3. As expected, the control antibody did not inhibit the hydrolysis (Figure 4d,e), supporting the specific interaction of LPL with PAP3 liposomes through its Trp-rich loop. Similarly, when a non-mammalian LPL (derived from *Burkholderia* sp.)—which lacks the conserved lipid binding domain of mammalian TGLs—was used with the 5D2 antibody (Figure S21 for complete sequence, Supporting Information), hydrolysis was not inhibited (Figure S22, Supporting Information), indicating again the specificity of 5D2 to the Trp-rich loop. Despite the hydrolysis of PAP3 liposomes taking place with the nonmammalian lipase, it appears to occur via a different mechanism, and it is therefore not relevant for the study of mammalian LPL species. It does however signify that 5D2 inhibits the Trp-loop specifically, and nonspecific interactions between antibody-protein-liposomes do not take place.

2.4. DOaG-DODAP Containing mRNA-LNPs Target and Transfect the bECs of Zebrafish Embryos

Aside from the mechanistic investigation and based on the selective in vivo behavior of PAP3 liposomes,^[15] we next investigated whether incorporating DOaG into mRNA-LNPs also results in selective cell targeting, as a novel approach for selective mRNA delivery and local protein expression (Figure 1c). An LNP formulation, based on standard lipid components, was modified with DOaG and the biodistribution, bEC targeting, and mRNA expression was examined in transgenic zebrafish embryos. Four LNP formulations were compared, and for this, two ionizable lipids were used (DODAP and the clinically approved MC3) and the structural lipid cholesterol was replaced with DOaG (Figure 5a; and Figure S23, Supporting Information). All formulations contained DSPC as the helper lipid, DMPE-PEG2k, and the far-red lipophilic dye DiD for fluorescent visualization. Functional mRNA expressing fluorescent reporter protein mCherry was used as cargo. The kdrl:GFP zebrafish line was used as fluorescent reference for vasculature visualization and colocalization studies. LNPs were fully characterized and found to have properties with comparable values in size, charge, polydispersity index (PDI), and encapsulation efficiency (Figure 5b). Hereafter, we use the following nomenclature for the four LNP formulations: LNP-A (i.e., CHO-DODAP), LNP-B (i.e., DOaG-DODAP), LNP-C (i.e., CHO-MC3), and LNP-D (i.e., DOaG-MC3).



Cryo-TEM and cryo-electron tomography (cryo-ET) was used to assess LNP ultrastructure and identify differences in morphology between all LNP formulations. For LNP-A, most of particles were either solid lipid particles, or particles with distinct lamellar compartments composed of a phospholipid bilayer (Figure 5c, black arrow; and Figure S24, Supporting Information). Such structures have been previously described as lipid “blebs” for LNP compositions similar to LNP-A and RNA has been found to localize in the “bleb’s” hydrophilic core.^[67,68] For LNP-A, a distinct punctuated electron-dense pattern is observed in the hydrophilic core of the bleb, indicating similarly mRNA localization (Figure 5c, red arrow). The morphology of LNP-C is characterized by solid lipid particles with a multilamellar lipid partitioning observed for some of the particles (Figure 5c; and Figure S24, Supporting Information). This type of morphology for this composition and similar molar ratios has been described before.^[69] Interestingly, the DOaG containing LNPs (LNP-B and LNP-D) were found to be solid, however a phase-separated droplet with different electron density was present within the particles (Figure 5c; and Figure S24, Supporting Information). Cryo-ET of LNP-B revealed the morphology in higher resolution (Figure 5c; and Movies S1–S3, Supporting Information). A similar morphology has been recently characterized, where cholesterol was replaced by its analogue fucosterol.^[70] It was suggested that phase separation may influence the mRNA localization toward the protruded area, however, no conclusive data were presented to support this claim. The electron density observed in the separate droplet in LNP-B and D is similar to the electron density induced when mRNA is present, therefore it seems to suggest that mRNA is present in the phase-separated droplet (see schematic in Figure 1c).

Next, formulations were intravenously (IV) administered in zebrafish (kdr1:GFP) at 3.5 days postfertilization (dpf) and imaged in real-time with confocal microscopy (Figure 5d). All formulations were predominantly in circulation 4 h postinjection (hpi) (Figure 5e; and Figure S25a,c,e,g, Supporting Information). To investigate bEC targeting in more detail, cellular localization of LNPs was studied by high resolution confocal z-stack imaging at the hindbrain, from a dorsal perspective (inset Figure 5d,f). LNP-A and C revealed to be circulating represented by a haze of fluorescence within the vasculature lumen (Figure 5f). Formulation LNP-D, also revealed to be circulating freely (Figure S25g, Supporting Information), however in a likely aggregated

state represented by clusters localized in the vasculature lumen (Figure 5f; and Figure S26b and Movie S4, Supporting Information). Strikingly, LNP-B revealed also strong fluorescent clusters, however these were localizing at the bECs, in contrast to LNP-D (Figure 5f; and Figure S26a and Movie S4, Supporting Information). Nonetheless, the combination of GFP-positive vasculature and far-red labeled LNPs allowed for quantification of their colocalization with bECs by using the Manders’ Overlap coefficient (MOC) (Figure 5g; and Figure S25b,d,f,h, Supporting Information).^[71] Quantification ($n = 3$) revealed that LNP-B localized preferentially at the bECs, compared to the other LNP formulations ($p < 0.01$). This suggests an important role for DOaG—in combination with DODAP—in LNP-mediated cell selective targeting. However, phase separation alone cannot explain bEC targeting—albeit it appears to be an important component for it—as cryo-TEM revealed similar phase-separated morphologies for LNP-B and LNP-D but different biodistribution profiles.

Next, we assessed whether bEC-targeting of LNP-B results in local expression of mCherry (Figure 5d). Whole fish and head were visualized for transfection at 36–38 hpi and DODAP containing formulations revealed overall relatively lower transfection levels in comparison to MC3 containing formulations (Figure S27a,b,d,e compared to Figure S27g,h,j,k, Supporting Information). We observed that LNP-C revealed high levels of transfection at the head and around the liver-swim bladder (Figure S27g,h, Supporting Information), but 3D imaging of the head revealed that mCherry expression was located at the exterior site of the brain, presumably at the skin (Movie S5, Supporting Information). Excitingly, LNP-B revealed relatively high mCherry expression levels in the brain region from both lateral and dorsal perspective (Figure S27d,e, Supporting Information). High resolution imaging of the brain vasculature confirmed selective transfection of the bECs, as evidenced by the colocalization of transgenic GFP-positive vasculature (kdr1:GFP) with mCherry expression (Figure 5h–j). Similar mCherry expression was observed in wild-type fish (ABTL) after 28hpi of LNP-B (Figure S28, Supporting Information). In contrast, LNP-A, C, and D did not seem to result in transfection in bECs, as evidenced by the relatively low mCherry fluorescence (Figure 5h). Quantification ($n = 9$) revealed that mCherry expression in bECs is significantly higher for LNP-B than LNP-A, C and D ($p < 0.01$, Figure 5k; and Figure S27c,f,i,l, Supporting Information). In summary, the

Figure 5. Physicochemical and in vivo evaluation of DOaG-containing mRNA-LNPs. a) Molar ratios of lipid components of the four mRNA-LNP formulations and information on functional mRNA, N/P ratio, and fluorescent tracer (constant for all LNP formulations). b) Size (average hydrodynamic diameter) and PDI as determined by DLS, surface charge as determined by zeta-potential measurements and mRNA encapsulation efficiency (%EE) as determined by IT-Ribogreen assay, for all mRNA-LNP formulations. c) Cryo-TEM images of all mRNA-LNP formulations and cryo-ET slices of LNP-B. Black arrow displays phospholipid bleb. Red and white arrows depict possibly encapsulated and free mRNA, respectively, as described before.^[67] Biodistribution of mRNA-LNPs within zebrafish embryos (3.5 dpf). d) Information and timeline of experimental setup. e) Lateral view on 3.5 dpf zebrafish embryo revealing DiD-represented biodistribution (4 hpi) as an overlay of LNP-B (magenta, single channel white) and GFP positive vasculature (green). Yellow box indicates region of brain vasculature. f) Dorsal view on brain vasculature at 4 hpi revealing biodistribution of LNP-A, LNP-B, LNP-C, and LNP-D. g) Quantification of Mander’s overlap coefficient (MOC) for DiD signal in relation to GFP-positive bECs. h) mCherry expression as a result of transfection for each formulation in the head region of the fish (confocal z-stacks of brain vasculature region). i) Overlay of mCherry expression (as mediated by LNP-B) and transgenic GFP positive vasculature. j) Inset of (i) depicting colocalization of GFP and mCherry (white arrows) and independent GFP fluorescence (gray arrows) indicating fluorescence as a result of transfection. k) Quantification of mCherry relative fluorescence intensity as result of bECs transfection, per formulation. The same LNP formulations (A–D) were used to produce all the data in the figure. Scale bars: 100 nm c), 500 μm e), 50 μm h,i,j), and 25 μm f). Statistical significance was evaluated as ns: not significant ($p > 0.05$), significantly different * $p < 0.05$, ** $p < 0.01$; *** $p < 0.001$. For g: note that B is significantly different to A, C, and D. Exact p -values: A-B = 0.0034, A-C = 0.0263, A-D = 0.3533, B-C = 0.0019, B-D = 0.0030, C-D = 0.3081. For k: note that B is significantly different to A, C, and D. Exact p -values: A-B = 0.0045, A-C = 0.0113, A-D = 0.0742, B-C = 0.0093, B-D = 0.0059, C-D = 0.3460.

phase-separated LNP-B formulation containing DOaG, targets, and transfects bECs preferentially as compared to the other formulations.

3. Discussion and Conclusion

In this work, we present the selective behavior of DOaG-containing lipid-based nanoparticles characterized by a selective membrane-protein communication and specific cell targeting. First, we investigate the influence of TGL on DOaG-containing liposomes. The liposomes, named PAP3, consist of the naturally occurring DSPC and the synthetic DAG analogue DOaG, which is responsible for the phase separation and constitution of a lipid droplet within each liposome bilayer. By combining experimental findings and MD simulation data we describe the selective lipolytic degradation of phase-separated lipid droplets in PAP3 liposomes upon incubation with LPL. We show LPL recognizes the enhanced lipid packing defects on the liposomal membrane induced by phase separation. PAP3 liposomes have been seen to interact with TGLs and specifically accumulate in cell subsets *in vivo*,^[15] a phenomenon attributed to their phase-separated morphology. Therefore, the observation of their structural evolution after interaction with LPL, as well as the mechanism of enzyme binding was of great interest. Here, we confirm the selective hydrolysis of DOaG by LPL, leading to degradation of the lipid droplet and to reorganization of the assembly to a lamellar bilayer, while the overall integrity of the nanoparticle is maintained. Contrarily, the other coformulant—DSPC—does not undergo hydrolysis. These observations exemplify selective nanoparticle-protein interactions and subsequent nanoparticle rearrangement. As TGLs endogenously remodel lipoproteins without nanoparticle collapse, i.e., LPL remodels very low-density lipoproteins to low-density lipoproteins^[38,72,73]—here we similarly show the depletion of a large part of the nanoparticle without bilayer disruption.

Additionally, we show that LPL is selective for PAP3 liposomes (DSPC/DOaG) and for liposomes containing the natural DAG counterpart (DSPC/DOG). LPL is not selective for 100% DSPC liposomes, or typical spherical LUVs with high circulation lifetimes *in vivo* (i.e., Myocet-like, POPC/CHO). One reason for this could be the inherent preference of LPL to hydrolyze DAGs and therefore DAG analogues, such as DOaG. Synergistically, another reason could be the preference of LPL to recognize membranes with high curvature—and thus higher packing defect constants—induced by phase separation.^[19,20,28] This hypothesis is supported by the nonlinear increased hydrolysis on liposomes consisting of $\geq 30\%$ DOaG (phase-separated), over liposomes consisting of $< 25\%$ mol DOaG (non phase-separated). Lipid packing defects were then quantified in our CGMD simulations and found to be higher when phase separation and high curvature are present in the membrane system. Finally, we show that LPL preferentially binds to the defected membrane of PAP3 liposomes, and we identified the Trp-rich loop of LPL as a lipid packing defect sensing motif. Preventing the Trp-loop to bind to PAP3 (by blocking the region with the selective antibody 5D2^[64]), abolishes the lipolysis and confirms the involvement of the Trp-rich loop in the recognition of PAP3 liposomes. Hereby, we expand our knowledge of the Trp-rich loop to act as a lipid packing defect sensor, beyond its role in lipoprotein binding.^[42] PAP3 li-

posomes, having lipid packing defects that arise upon phase separation, appear to hijack the natural pathway in which LPL recognizes lipoproteins via its Trp-rich loop.

Additionally, we have previously shown PAP3 liposomes to be endocytosed by a TGL-mediated pathway *in vivo*.^[15] A possible pathway for this could be the selective recognition of DOaG by TGL—with a significantly higher chance of DOaG being transiently exposed to the aqueous environment due to the increased packing defects in the phase-separated membrane—and subsequent endocytosis. Our current study shows the selective lipolysis and remodeling of the particle by LPL, something that may also occur *in vivo* before nanoparticle uptake by the cell. However, given the complex *in vivo* environment and the spatiotemporal regulation of lipase function in lipid metabolism, further studies should be performed *in vivo* and in real-time to solidly prove this hypothesis. Here, it should be noted, apolipoprotein CII (APOCII) is an essential cofactor of LPL and, in a physiological environment, it will play a central role on efficient lipase activity.^[34] This is an aspect that is not presented in the current study. However, the presence of apolipoproteins is not vital for LPL binding on lipid membranes^[42] and, although APOCII would enhance the LPL lipolytic efficiency (or would even be essential in an *in vivo* environment), it is not required for overall LPL activity; especially not for comparison of relative activity on different targets (i.e., different liposomal formulations).

In the case of *in vivo* selective lipolysis of the PAP3 lipid droplet—without nanoparticle collapse as this study suggests—, these nanoparticles can exert unique properties for drug delivery, i.e., the lipid droplet could be used as a guide “moiety” for cell selective accumulation through a lipase-mediated pathway, while the hydrophilic core could incorporate functional drugs. Alternatively, pro-drugs could be incorporated within the lipid droplet, exploiting the selective lipase interaction for specific drug release, i.e., lipase-mediated prodrug hydrolysis and subsequent drug release.

Another noteworthy observation is the visible remnants of the hydrolyzed droplet on some nanoparticles (Figure S29, arrows, Supporting Information). Such thickness mismatches in cryo-TEM have been recently described as nanodomains in liposomal membranes.^[74,75] Therefore, although PAP3 liposomes can be seen as lamellar and nonphase separated macromolecularly after LPL incubation, a more in-depth investigation of the molecular details is required, e.g., the existence of nanodomains or lipid rafts remaining after LPL hydrolysis. The question that arises here is whether such nanodomains can be still recognizable by TGLs *in vivo*.

Finally, as mentioned earlier, the selection of LPL as a representative TGL was purely due to the extensive literature on LPL structure, regulation, and function in health and disease, and therefore was the most relevant protein to base our studies on. However, all (mammalian) lipases from the TGL family have very similar amino acid sequences⁽⁴⁰⁾ and Figure S30 for protein alignment, Supporting Information), structural homology, and similar functional roles on triglyceride metabolism.^[37,76–78] This allows the assumption that other TGLs will behave similarly on PAP3 liposomes as the LPL studied here. On the same note, the LPL chosen for these studies was derived from bovine milk (*Bos Taurus*), yet the sequence homology with human LPL (*Homo Sapiens*) is $> 90\%$, with high structural similarity and a

conserved Trp-loop (see Figures S31 and S32 for protein structure alignment, Supporting Information), which allows to assume that it will similarly affect PAP3 liposomes as bovine LPL. To support this, we show that incubating PAP3 liposomes with human LPL releases a substantial amount of FFA (Figure S33, Supporting Information). Also, similar PMF profiles were calculated for human LPL interacting with the DOaG/DSPC phase-separated membrane and a flat DSPC bilayer through its Trp-rich loop, showing even a more substantial binding preference for the phase-separated system in terms of the free energy difference between the minima ($13.48 \text{ kJ mol}^{-1}$) (Figure S34, Supporting Information).

Overall, this study explains in detail the how and the why of the preferential interaction of TGLs with unique phase-separated liposomes. Such interaction has been recently found responsible for cell specific targeting in vivo.^[15] Particularly, it serves an important proof-of-concept for selective protein interaction on lipid nanoparticle membranes, owing to lipid packing defects.

Finally, we show that DOaG-induced phase separation in membranes can also be used to deliver mRNA cell-selectively in vivo, by the development of a second-generation of DOaG-containing LNP formulation. Exchanging cholesterol with DOaG in a standard LNP formulation (denoted LNP-B), resulted in selective LNP-B accumulation in bECs of zebrafish embryos, indicating a potential role of DOaG for the selective targeting. Switching one only lipid component dramatically affected the LNP biodistribution toward bECs (i.e., DOaG vs cholesterol). Similarly, replacing DODAP with MC3 resulted in a formulation (LNP-D) that cannot achieve cell specific targeting, most probably due to colloidal instability. Therefore, to achieve cell selectivity, in vivo LNP colloidal stability is an important parameter. We hypothesize that there is a molecular difference between LNP-B and LNP-D that is beyond the resolution of cryo-TEM that could contribute to the clustering of LNP-D preventing accumulation in bECs. Further studies are required to elucidate the mechanism of targeting and whether the phase-separated LNP morphology is essential.

Nonetheless, the DOaG-containing LNP-B formulation provides evidence and supports the hypothesis that exploiting DOaG and the related phase separation, can be translated from liposomes to LNPs, resulting in selective in vivo behavior and unlocking the potential of selective RNA in vivo delivery.

DAGs (and analogues) are lipids with several interesting properties including fusion promotion, polymorphism, and protein recruitment.^[79] All these properties render DAGs as interesting molecules for lipid-based nanoparticle formulations, nevertheless, have not been widely explored. One potential advantage of using DAGs as lipid components in lipid-based nanoparticles, is their propensity to form liquid crystalline phases (i.e., inverse hexagonal phase [H_{II}]) which can promote fusion and potentially facilitate endosomal escape, leading to higher transfection efficiencies.^[70,80–82] Also, their general ability to induce phase separation in lipid-based nanoparticles could propel higher transfection potencies, similar to recently described phase-separated blebs in LNP systems.^[83]

Overall, the selective nano-bio interactions presented in this study emphasize the importance of understanding how lipid composition affects physicochemical properties and overall

nanoparticle behavior. Persistent and limited understanding of the key nano-bio interactions of nanoparticles has so far stymied progression from empirical discovery toward rational nanoparticle design, an aspect that could lead to more advanced and precise nanomedicines in the future.

4. Experimental Section

Liposome Formulation: Large unilamellar vesicles (LUVs) were formed through extrusion (mini extruder, Avanti Polar Lipids) above the T_m of all lipids (i.e., $65\text{--}70^\circ\text{C}$) in 10 mM Tris Buffer pH 7.4 and at a total lipid concentration of 5 mM (3.5 mg mL^{-1}), unless if stated otherwise. Individual lipids as stock solutions (10 mM) in chloroform, were combined to the desired molar ratios and dried to a thin film, first under N_2 stream, then $>1 \text{ h}$ under vacuum. Lipid films were hydrated with 1 mL Tris Buffer above the T_m of all lipids ($65\text{--}70^\circ\text{C}$), with gentle vortexing, to form a suspension. Hydrated lipids were passed 11 times through $2 \times 400 \text{ nm}$ polycarbonate (PC) membranes (Nucleopore Track-Etch membranes, Whatman), followed by 11 times through $2 \times 100 \text{ nm}$ PC membranes. All liposomes were stored at 4°C and used within 5 days.

Liposome–Lipase Incubation: Liposomes (3.5 mg mL^{-1} , in 10 mM Tris Buffer, pH 7.4) were transferred in a low protein binding tube (3 mg mL^{-1} final lipid concentration after lipase incubation) and subsequently Lipoprotein Lipase (in 10 mM Tris Buffer pH 7.4) was added to the tube to reach 0.03 mg mL^{-1} final concentration. Liposomes–lipase mixture was left to incubate at 37°C in a thermomixer for up to 20 h with gentle occasional mixing.

LNP Formulation: Encapsulation of mRNA and simultaneous formation of lipid nanoparticles in a Nitrogen to Phosphate ratio (N/P ratio) of 6, was performed as previously described.^[84] In brief, individual lipid components (DSPC, DMPE-PEG2k, DOaG, or cholesterol, DODAP or MC3) as stock solutions in chloroform (1–10 mM), were combined to the desired molar ratios and dried to ensure complete removal of chloroform, first under a stream of N_2 , then $>1 \text{ h}$ under vacuum. The nonexchangeable tracer DiD was also added to the lipid mixtures at a total lipid concentration of 0.1% mol. Lipid films were redissolved (with vortexing) in 200 μL of absolute ethanol at a total lipid concentration of 5.31 mM. In another vial, 30 μL of mRNA encoding mCherry (1 mg mL^{-1}) were diluted up to 600 μL with nuclease-free sodium citrate buffer (pH 4.0, 16.7 mM trisodium citrate dihydrate and 30.5 mM citric acid monohydrate). Controlled rapid mixing of the two solutions was achieved by using a custom-made T-junction mixer, equipped with syringe pumps (fusion 100-X, Chemyx Inc., Stafford, USA) and syringes with an inner diameter of 4.78 mm. The total flow rate was 2 mL min^{-1} , with a flow rate ratio of 3:1 v/v citrate buffer: ethanol). The resulting LNP formulations were dialyzed overnight against nuclease-free PBS (pH 7.4). LNP formulations were concentrated at 4°C to the lowest volume possible by centrifugation at 2000–3000 g using 100 K MWCO centrifugal filters (Amicon Ultra, Merck) resulting in mRNA-LNPs with [total lipid] $\approx 16\text{--}18 \text{ mM}$. Microfluidic mixing and mRNA were handled with nuclease-free lab consumables and gloves throughout.

Cryogenic Transmission Electron Microscopy: Freshly glow-discharged carbon grids supported on Cu (Lacey carbon film, 200 mesh, Electron Microscopy Sciences, Aurion, The Netherlands) were used for vitrification inside a Vitrobot plunge-freezer (FEI VitrobotTM Mark III, Thermo Fisher Scientific) regulating steady temperature and humidity conditions (22 or 37°C and 99% humidity). Liposomes incubating with LPL at 37°C were immediately taken and applied to the grid and the excess liquid was blotted for 3 s and subsequently plunge frozen in liquid ethane below -160°C to ensure formation of vitreous ice. mRNA-LNP formulations ($3.5 \mu\text{L}$) were applied to a grid and blotted for 3 s at 99% humidity with a waiting time of 30 s before blotting. Cryo-TEM images were collected on a Talos L120C (NeCEN, Leiden University) operating at 120 kV or on a Titan Krios (TU Eindhoven) operating at 300 kV, with working temperature below -180°C . Images were recorded manually at a nominal magnification of 1100x, 13 500x, 22 000x, 28 000x, or 36 000x yielding a pixel size at the specimen of 9.47, 7.41, 4.44, 3.46, or 2.86 \AA , respectively.

Simulation Details: All simulations were performed with GROMACS 2019.3^[85] and the Martini 3.0.0 force field^[53] at a 20 fs time step. Temperature ($T = 303.15$ K, $\tau_T = 1$ ns) and pressure coupling (compressibility = 4.5×10^{-5} bar⁻¹, $\tau_p = 12$ ns) were applied by the velocity rescaling thermostat and the Berendsen barostat, respectively. The neighbor list was updated every 20 steps. A 1.1 nm cutoff was used for the Van der Waals interactions (shifted Verlet cutoff scheme) and Coulomb interactions (reaction-field electrostatics).

Coarse-Grained Model for PAP3 Liposomes: Phase separation on PAP3 liposomes was determined from the MD trajectories, using the time-averaged contact fraction between the DOaG and the DSPC lipid. Following a general procedure,^[54] a relative contact fraction was calculated by counting contacts between DOaG and DSPC lipids and dividing it by the total number of DOaG contacts (see Sections S12–S15 for details, Supporting Information). A cutoff of 1.1 nm was used to identify contacts between lipids via selected beads on both lipid types that are roughly at the same depth within the membrane. In addition, it was normalized by the total concentration of DOaG to enable direct comparison for different DoaG concentrations. Consequently, complete phase separation always corresponds to a value of zero, and ideal mixing to unity.

Droplet Simulation: For the simulation of the droplet, the droplet configuration was made with PackMol^[86] with—on the inside—purely DoaG and on the outside a monolayer of DSPC. The simulated annealing was run for 1.5 μ s, with a starting temperature of 450 K and cooled to a temperature of 303 K, after which the temperature was kept stable for 500 ns at the final temperature. After the simulated annealing the droplet was ran for analysis for 1.5 μ s at the same temperature and settings as the bilayer simulations.

Packing Defects: While previous work used the PackMem package^[87] to identify a linearly increasing defect size constant with total curvature for both single component and mixed membranes^[23] the role of (de)mixing remains less quantified. Here, a new computational protocol was developed to clarify this relation for the highly curved DOaG/DSPC membranes of arbitrary (nonsymmetric) shapes. Packing defect constants for the simulated PAP3 droplet can in principle be determined using standard PackMem routines, by employing a spherical instead of the usual rectangular grid.^[23] However, since droplets do not necessarily adopt a purely spherical shape, even tiny mismatches in the determination of the relevant reference interface may bias the calculated constants in a nonpredictable fashion. For this reason, a protocol was developed that can deal with arbitrary shapes. Briefly, a closed 2D interface is fitted through the positions of relevant GL beads, subsequently triangulated, and used as a reference for identifying shallow and deep defects following the recommended PackMem settings.^[87] Details and examples of this procedure will be published in a separate study.

Protein Modeling and Lipid Packing Defect Sensing Prediction: The 3D models of human and bovine LPL were downloaded from the AlphaFold2 database.^[88,89] Both structures closely overlap with the human crystal structure^[56] (Figure S32, Supporting Information). The unstructured N-terminal signal sequence (residue 1–34) was excluded. To predict which regions of the protein may play a role in lipid packing defect sensing, a previously developed neural network model was applied.^[59] A sliding window of 15 residues was used to predict $\Delta\Delta F$ values for peptide motifs along the sequence of the bovine LPL protein (Section S17–S19, Supporting Information). In order to exclude buried protein regions (that are unavailable to interact with membranes), only peptide motifs with an average solvent-accessible surface area (SASA, as calculated using BioPython^[90]) of greater than 0.8 nm² were considered. To visualize putative regions of interest, the B-factor field in the PDB file format was used to adjust the coloring accordingly.

Umbrella Sampling: A DSPC bilayer (361 molecules per leaflet) was prepared using the insane python script^[91] and the Martini 3 CG force field.^[53] After solvation with Martini 3 water and ions (0.15 M NaCl), steepest decent energy minimization and 10 ns of semiisotropic NpT equilibration ($p_{ref} = 1$ bar) were performed. Next, a layer of 1444 randomly oriented DOaG molecules was inserted between the two DSPC leaflets. The resulting 1:2 DSPC:DOaG membrane was energy minimized and equilibrated. A 75 bar nm surface tension was applied to the mem-

brane system to match the lipid packing defects (measured with a protocol based on PackMem (same as the one calculating defects on the spherical droplet and with the recommended settings^[87]) to the ones found on a DSPC/DOaG spherical lipid droplet (see Figure S16, Supporting Information). A CG Martini representation of the LPL protein was obtained with Martinize2/VerMOUTH.^[92] Secondary structure was predicted with DSSP^[93] and constrained by an elastic network between the backbone beads ($k_{force} = 500$ kJ mol⁻¹). The CG protein was inserted into the DSPC/DSPC-DOaG systems with ≈ 4 nm separation between the Trp-rich loop of the protein (Ile413-Pro427) and the upper leaflet's lipid head groups. The resulting set-ups were resolvated with water and ions (0.15 M NaCl). After steepest decent energy minimization, both systems were equilibrated for 100 ns with position restraints ($k_{force} = 1000$ kJ mol⁻¹) on all protein beads. The initial frames for US were generated by running a pulling simulation in which the z-distance between the centers-of-mass (COM) of the Trp-rich loop and the lipids was decreased gradually, and then selecting 24 frames that span the range from the solvated to the membrane-bound state with 0.2 nm increments. For each umbrella window, a 50 ns equilibration followed by a 2 μ s production run was performed in which the Lipid-Trp-rich loop COM z-distance was constrained to its initial value ($k_{force} = 500$ kJ mol⁻¹). To dampen membrane deformations during US runs, a soft harmonic flat-bottom potential ($k_{force} = 100$ kJ mol⁻¹) was applied on the lipid head groups to restrain the lipids within its initial thickness range (+0.5 nm on each side of the membrane). Free energy profiles were obtained through umbrella integration^[94] with 10 000 bins. Averages and standard deviations were calculated by using block-averaging over 3 blocks.

Zebrafish Husbandry and Injections: Zebrafish (Danio rerio, Tg (kdr:l:GFP)s843)^[95] were, in compliance with the directives of the local animal welfare committee of Leiden University, handled and maintained according to Zebrafish Model Organism Database guidelines (<http://zfin.org>, 2023). Natural spawning at beginning of light period was used for fertilized egg collection, which were subsequently grown at 28.5 °C in egg water (60 g mL⁻¹ Instant Ocean Sea salts). Zebrafish embryos were anesthetized and embedded in 0.4% w/v agarose containing 0.01% tricaine. Screening studies from injection to image analysis were kept blind. Formulations were injected in the Duct of Cuvier at 3.5 dpf stage as previously described^[49] (V injection = 1 nL volume, [mRNA] = 0.2 mg mL⁻¹ per embryo). Zebrafish were qualified as correctly injected when formulation fluorescence correlated with vasculature and no backward translocation of erythrocytes and/or yolk damage was detected. Fish were randomly selected from a group of correctly injected embryos. Confocal microscopy was performed at 4 and 36–38 hpi and embryos were imaged by overlapping z-plane. Images for quantification were performed using a Leica TCS SP8 confocal microscope, with a 40X water-immersion objective (HCX APO L) and photon count as detection method. Laser intensity, gain, and offset settings were kept identical for unbiased quantification.

Supporting Information

Supporting Information is available from the Wiley Online Library or from the author.

Acknowledgements

P.P., R.v.d.P., N.v.H., and W.L.v.O. contributed equally to this work. This work was supported by a Leiden/Huygens Scholarship grant supporting P.P. This work was also supported by the Deutsche Forschungsgemeinschaft (DFG, German Research Foundation) under Germany's Excellence Strategy – EXC 2033 – 390677874 – RESOLV. The authors also thanked the NWO Vidi scheme (Project No. 723.016.005), and the DFG (Grant No. RI2791/2-1) for funding H.J.R. and N.v.H. This work was also benefited from access to the Netherlands Centre for Electron Nanoscopy (NeCEN) at Leiden University, an Instruct-ERIC center, with technical assistance from Ludovic Renault and Birgit Luef. The Dutch Research Organization NWO (Snellius@Surfsara) and the HLRN Göttingen/Berlin are acknowledged for the provided computational resources. The authors would like

to thank Aleksandra Chikunova for fruitful discussions during this project, and Bjor de Wit whose M.Sc. thesis project helped shaping the research presented here through its initial stages.

Note: Labelling in Figure 5i and the formatting of the author name Nico Sommerdijk were corrected on January 12, 2024 after initial publication online.

Conflict of Interest

The authors declare no conflict of interest.

Data Availability Statement

The data that support the findings of this study are available from the corresponding author upon reasonable request.

Keywords

cell targeting, lipases, lipid-based nanoparticles, mRNA-delivery, nano-bio interface, phase-separated

Received: October 18, 2023

Published online: December 6, 2023

- [1] U. Bulbake, S. Doppalapudi, N. Kommineni, W. Khan, *Pharmaceutics* **2017**, *9*, 12.
- [2] P. R. Cullis, M. J. Hope, *Mol. Ther.* **2017**, *25*, 1467.
- [3] A. Akinc, M. A. Maier, M. Manoharan, K. Fitzgerald, M. Jayaraman, S. Barros, S. Ansell, X. Du, M. J. Hope, T. D. Madden, B. L. Mui, S. C. Semple, Y. K. Tam, M. Ciufolini, D. Witzigmann, J. A. Kulkarni, R. Van Der Meel, P. R. Cullis, *Nat. Nanotechnol.* **2019**, *14*, 1084.
- [4] J. A. Kulkarni, M. M. Darjuan, J. E. Mercer, S. Chen, R. Van Der Meel, J. L. Thewalt, Y. C. Tam, P. R. Cullis, *ACS Nano* **2018**, *12*, 4787.
- [5] L. Schoenmaker, D. Witzigmann, J. A. Kulkarni, R. Verbeke, G. Kersten, W. Jiskoot, D. J. Crommelin, *Int. J. Pharm.* **2021**, *601*, 120586.
- [6] X. Hou, T. Zaks, R. Langer, Y. Dong, *Nat. Rev. Mater.* **2021**, *6*, 1078.
- [7] T. Lammers, F. Kiessling, W. E. Hennink, G. Storm, *J. Controlled Release* **2012**, *161*, 175.
- [8] A. Tewabe, A. Abate, M. Tamrie, A. Seyfu, E. Abdela Siraj, *J. Multidiscip. Healthcare* **2021**, *14*, 1711.
- [9] V. Francia, R. M. Schifferlers, P. R. Cullis, D. Witzigmann, *Bioconjug. Chem.* **2020**, *31*, 2046.
- [10] R. Pattipeiluhu, S. Crielgaard, I. Klein-Schiphorst, B. I. Florea, A. Kros, F. Campbell, *ACS Cent. Sci.* **2020**, *6*, 535.
- [11] M. Hadjidemetriou, S. Mcadam, G. Garner, C. Thackeray, D. Knight, D. Smith, Z. Al-Ahmady, M. Mazza, J. Rogan, A. Clamp, K. Kostarelos, *Adv. Mater.* **2019**, *31*, 1803335.
- [12] M. Hadjidemetriou, K. Kostarelos, *Nat. Nanotechnol.* **2017**, *12*, 288.
- [13] M. N. Holme, M. H. Rashid, M. R. Thomas, H. M. G. Barriga, K. L. Herpoldt, R. K. Heenan, C. A. Dreiss, J. L. Bañuelos, H. N. Xie, I. Yarovsky, M. M. Stevens, *ACS Cent. Sci.* **2018**, *4*, 1023.
- [14] W.-K. Fong, A. Sánchez-Ferrer, M. Rappolt, B. J. Boyd, R. Mezzenga, *Langmuir* **2019**, *35*, 14949.
- [15] G. Arias-Alpizar, P. Papadopoulou, X. Rios, K. R. Pulagam, M.-A. Moradi, R. Pattipeiluhu, J. Bussmann, N. Sommerdijk, J. Llop, A. Kros, F. Campbell, *Adv. Healthcare Mater.* **2023**, *12*, 2202709.
- [16] P. Campomanes, V. Zoni, S. Vanni, *Commun. Chem.* **2019**, *2*, 72.
- [17] M. Alwarawrah, F. Hussain, J. Huang, *Biochim. Biophys. Acta Biomembr.* **2016**, *1858*, 253.
- [18] E. J. Bolen, J. J. Sando, *Biochemistry* **1992**, *31*, 5945.
- [19] F. M. Goñi, A. Alonso, *Prog. Lipid Res.* **1999**, *38*, 1.
- [20] E. M. Goldberg, D. S. Lester, D. B. Borchardt, R. Zidovetzki, *Biophys. J.* **1995**, *69*, 965.
- [21] C. R. Coffill, T. A. Ramsamy, D. M. Hutt, J. R. Schultz, D. L. Sparks, *J. Lipid Res.* **1997**, *38*, 2224.
- [22] C. Vieu, B. Jaspard, R. Barbaras, J. Manent, H. Chap, B. Perret, X. Collet, *J. Lipid Res.* **1996**, *37*, 1153.
- [23] S. Vanni, H. Hirose, H. Barelli, B. Antonny, R. Gautier, *Nat. Commun.* **2014**, *5*, 4916.
- [24] M. Alwarawrah, J. Dai, J. Huang, *J. Chem. Theory Comput.* **2012**, *8*, 749.
- [25] E. M. Goldberg, D. S. Lester, D. B. Borchardt, R. Zidovetzki, *Biophys. J.* **1994**, *66*, 382.
- [26] L. Vamparys, R. Gautier, S. Vanni, W. F. D. Bennett, D. P. Tieleman, B. Antonny, C. Etchebest, P. F. J. Fuchs, *Biophys. J.* **2013**, *104*, 585.
- [27] G. Drin, J.-F. Casella, R. Gautier, T. Boehmer, T. U. Schwartz, B. Antonny, *Nat. Struct. Mol. Biol.* **2007**, *14*, 138.
- [28] N. S. Hatzakis, V. K. Bhatia, J. Larsen, K. L. Madsen, P.-Y. Bolinger, A. H. Kunding, J. Castillo, U. Gether, P. Hedegård, D. Stamou, *Nat. Chem. Biol.* **2009**, *5*, 835.
- [29] S. Vanni, L. Vamparys, R. Gautier, G. Drin, C. Etchebest, P. F. J. Fuchs, B. Antonny, *Biophys. J.* **2013**, *104*, 575.
- [30] K. D. Wildermuth, V. Monje-Galvan, L. M. Warburton, J. B. Klauda, *J. Chem. Theory Comput.* **2019**, *15*, 1418.
- [31] S. Kim, M. I. Oh, J. M. J. Swanson, *J. Phys. Chem. B* **2021**, *125*, 5572.
- [32] A. Barlič, I. Gutié rrez-Aguirre, J. M. M. Caaveiro, A. Cruz, M.-B. Ruiz-Argü ello, J. Pé rez-Gil, *J. Biol. Chem.* **2004**, *279*, 34209.
- [33] H. Ahyauch, J. Sot, M. I. Collado, N. Huarte, J. Requejo-Isidro, A. Alonso, F. M. Goñi, *Biophys. J.* **2015**, *108*, 1672.
- [34] S. S.-R. Bohr, C. Thorlaksen, R. M. Kühnel, T. Günther-Pomorski, N. S. Hatzakis, *Langmuir* **2020**, *36*, 6473.
- [35] I. V. Fuki, N. Blanchard, W. Jin, D. H. L. Marchadier, J. S. Millar, J. M. Glick, D. J. Rader, *J. Biol. Chem.* **2003**, *278*, 34331.
- [36] M. Merkel, Y. Kako, H. Radner, I. S. Cho, R. Ramasamy, J. D. Brunzell, I. J. Goldberg, J. L. Breslow, *PNAS* **1998**, *95*, 13841.
- [37] P. W. Connelly, *Clin. Chim. Acta* **1999**, *286*, 243.
- [38] J. Mead, S. Irvine, D. Ramji, *J. Mol. Med.* **2002**, *80*, 753.
- [39] M. Jaye, K. J. Lynch, J. Krawiec, D. Marchadier, C. Maugeais, K. Doan, V. South, D. Amin, M. Perrone, D. J. Rader, *Nat. Genet.* **1999**, *21*, 424.
- [40] Z. Wang, S. Li, L. Sun, J. Fan, Z. Liu, *PLoS One* **2013**, *8*, e72146.
- [41] S. Y. Choi, K.-I. Hirata, T. Ishida, T. Quertermous, A. D. Cooper, *J. Lipid Res.* **2002**, *43*, 1763.
- [42] A. Lookene, N. B. Groot, J. J. P. Kastelein, G. Olivecrona, T. Bruin, *J. Biol. Chem.* **1997**, *272*, 766.
- [43] S. E. Williams, I. Inoue, H. Tran, G. L. Fry, M. W. Pladet, P. H. Iverius, J. M. Lalouel, D. A. Chappell, D. K. Strickland, *J. Biol. Chem.* **1994**, *269*, 8653.
- [44] C. N. Goulbourne, P. Gin, A. Tatar, C. Nobumori, A. Hoenger, H. Jiang, C. R. M. Grovenor, O. Adeyo, J. D. Esko, I. J. Goldberg, K. Reue, P. Tontonoz, A. Bensadoun, A. P. Beigneux, S. G. Young, L. G. Fong, *Cell Metab.* **2014**, *19*, 849.
- [45] J. E. Yu, S. Y. Han, B. Wolfson, Q. Zhou, *Histol. Histopathol.* **2018**, *33*, 1.
- [46] J. Borén, A. Lookene, E. Makoveichuk, S. Xiang, M. Gustafsson, H. Liu, P. Talmud, G. Olivecrona, *J. Biol. Chem.* **2001**, *276*, 26916.
- [47] F. H. De Man, F. De Beer, A. Van Der Laarse, A. H. Smelt, L. M. Havekes, *J. Lipid Res.* **1997**, *38*, 2465.
- [48] G. Perdomo, D. H. Kim, T. Zhang, S. Qu, E. A. Thomas, F. G. S. Toledo, S. Slusher, Y. Fan, D. E. Kelley, H. H. Dong, *J. Lipid Res.* **2010**, *51*, 1298.

- [49] F. Campbell, F. L. Bos, S. Sieber, G. Arias-Alpizar, B. E. Koch, J. Huwyler, A. Kros, J. Bussmann, *ACS Nano* **2018**, *12*, 2138.
- [50] G. Batist, J. Barton, P. Chaikin, C. Swenson, L. Welles, *Expert Opin Pharmacother* **2002**, *3*, 1739.
- [51] S. Sun, R. Dean, Q. Jia, A. Zenova, J. Zhong, C. Grayson, C. Xie, A. Lindgren, P. Samra, L. Sojo, M. van Heek, L. Lin, D. Percival, J. M. Fu, M. D. Winther, Z. Zhang, *Bioorg. Med. Chem.* **2013**, *21*, 7724.
- [52] M. Rigoni, P. Caccin, S. Gschmeissner, G. Koster, A. D. Postle, O. Rossetto, G. Schiavo, C. Montecucco, *Science* **2005**, *310*, 1678.
- [53] P. C. T. Souza, R. Alessandri, J. Barnoud, S. Thallmair, I. Faustino, F. Grünwald, I. Patmanidis, H. Abdizadeh, B. M. H. Bruininks, T. A. Wassenaar, P. C. Kroon, J. Melcr, V. Nieto, V. Corradi, H. M. Khan, J. Domanski, M. Javanainen, H. Martinez-Seara, N. Reuter, R. B. Best, I. Vattulainen, L. Monticelli, X. Periole, D. P. Tieleman, A. H. De Vries, S. J. Marrink, *Nat. Methods* **2021**, *18*, 382.
- [54] Y. Liu, A. H. De Vries, W. Pezeshkian, S. J. Marrink, *J. Chem. Theory Comput.* **2021**, *17*, 5876.
- [55] N. Van Hilten, K. S. Stroh, H. J. Risselada, *J. Chem. Theory Comput.* **2022**, *18*, 4503.
- [56] R. Arora, A. v. Nimonkar, D. Baird, C. Wang, C. H. Chiu, P. A. Horton, S. Hanrahan, R. Cubbon, S. Weldon, W. R. Tschantz, S. Mueller, R. Brunner, P. Lehr, P. Meier, J. Ottl, A. Voznesensky, P. Pandey, T. M. Smith, A. Stojanovic, A. Flyer, T. E. Benson, M. J. Romanowski, J. W. Trauger, *PNAS* **2019**, *116*, 10360.
- [57] K. H. Gunn, B. S. Roberts, F. Wang, J. D. Strauss, M. J. Borgnia, E. H. Egelman, S. B. Neher, *PNAS* **2020**, *117*, 10254.
- [58] H. Wong, R. C. Davis, T. Thuren, J. W. Goers, J. Nikazy, M. Waite, M. C. Schotz, *J. Biol. Chem.* **1994**, *269*, 10319.
- [59] N. Van Hilten, J. Methorst, N. Verwei, H. J. Risselada, *Sci. Adv.* **2023**, *9*, eade8839.
- [60] H. Cui, E. Lyman, G. A. Voth, *Biophys. J.* **2011**, *100*, 1271.
- [61] S. Antamarina-Fojo, K. A. Dugi, *Curr. Opin. Lipidol.* **1994**, *5*, 117.
- [62] C. Prévost, M. E. Sharp, N. Kory, Q. Lin, G. A. Voth, R. V. Farese, T. C. Walther, *Dev. Cell* **2018**, *44*, 73e4.
- [63] S. Kim, J. M. J. Swanson, G. A. Voth, *J. Phys. Chem. B* **2022**, *126*, 2145.
- [64] J. G. Luz, A. P. Beigneux, D. K. Asamoto, C. He, W. Song, C. M. Allan, J. Morales, Y. Tu, A. Kwok, T. Cottle, M. Meiyappan, L. G. Fong, J. E. Kim, M. Ploug, S. G. Young, G. Birrane, *J. Lipid Res.* **2020**, *61*, 1347.
- [65] S.-F. Chang, B. Reich, J. D. Brunzell, H. Will, *J. Lipid Res.* **1998**, *39*, 2350.
- [66] K. K. Kristensen, K. Z. Leth-Espensen, H. D. T. Mertens, G. Birrane, M. Meiyappan, G. Olivecrona, T. J. D. Jørgensen, S. G. Young, M. Ploug, *PNAS* **2020**, *117*, 4337.
- [67] M. L. Brader, S. J. Williams, J. M. Banks, W. H. Hui, Z. H. Zhou, L. Jin, *Biophys. J.* **2021**, *120*, 2766.
- [68] A. K. K. Leung, Y. Y. C. Tam, S. Chen, I. M. Hafez, P. R. Cullis, *J. Phys. Chem. B* **2015**, *119*, 8698.
- [69] M. Y. Arteta, T. Kjellman, S. Bartesaghi, S. Wallin, X. Wu, A. J. Kvist, A. Dabkowska, N. Székely, A. Radulescu, J. Bergenholtz, L. Lindfors, *PNAS* **2018**, *115*, E3351.
- [70] Y. Eygeris, S. Patel, A. Jozic, G. Sahay, *Nano Lett.* **2020**, *20*, 4543.
- [71] E. M. M. Manders, F. J. Verbeek, J. A. Aten, *J. Microsc.* **1993**, *169*, 375.
- [72] S. A. Wu, S. Kersten, L. Qi, *Trends Endocrinol. Metab.* **2021**, *32*, 48.
- [73] S. Kersten, *Biochim. Biophys. Acta* **2014**, *1841*, 919.
- [74] C. E. Cornell, A. Mileant, N. Thakkar, K. K. Lee, S. L. Keller, *PNAS* **2020**, *117*, 19713.
- [75] F. A. Heberle, M. Doktorova, H. L. Scott, A. D. Skinkle, M. N. Waxham, I. Levental, *PNAS* **2020**, *117*, 19943.
- [76] S. A. Khetarpal, C. Vitali, M. G. Levin, D. Klarin, J. Park, A. Pampana, J. S. Millar, T. Kuwano, D. Sugasini, P. v. Subbaiah, J. T. Billheimer, P. Natarajan, D. J. Rader, *PLoS Genet.* **2021**, *17*, 1009802.
- [77] G. Olivecrona, T. Olivecrona, *Curr. Opin. Lipidol.* **2010**, *21*, 409.
- [78] M. J. Watt, L. L. Spriet, *Am. J. Physiol. Endocrinol. Metab.* **2010**, *299*, E162.
- [79] J. C. Gómez-Fernández, S. Corbalán-García, *Chem. Phys. Lipids* **2007**, *148*, 1.
- [80] B. G. Tenchov, R. C. Macdonald, D. P. Siegel, *Biophys. J.* **2006**, *91*, 2508.
- [81] S. L. Veatch, S. L. Keller, *Biophys. J.* **2003**, *85*, 3074.
- [82] S. Patel, N. Ashwanikumar, E. Robinson, Y. Xia, C. Mihai, J. P. Griffith, S. Hou, A. A. Esposito, T. Ketova, K. Welscher, J. L. Joyal, Ö. Almarsson, G. Sahay, *Nat. Commun.* **2020**, *11*, 983.
- [83] M. H. Y. Cheng, J. Leung, Y. Zhang, C. Strong, G. Basha, A. Momeni, Y. Chen, E. Jan, A. Abdolazadeh, X. Wang, J. A. Kulkarni, D. Witzigmann, P. R. Cullis, *Adv. Mater.* **2023**, *35*, 2303370.
- [84] R. Pattipeiluhu, G. Arias-Alpizar, G. Basha, K. Y. T. Chan, J. Bussmann, T. H. Sharp, M.-A. Moradi, N. Sommerdijk, E. N. Harris, P. R. Cullis, A. Kros, D. Witzigmann, F. Campbell, *Adv. Mater.* **2022**, *34*, 2201095.
- [85] M. J. Abraham, T. Murtola, R. Schulz, S. Páll, J. C. Smith, B. Hess, E. G. Lindahl, *SoftX* **2015**, *1*, 19.
- [86] L. Martínez, R. Andrade, E. G. Birgin, J. M. Martínez, *J. Comput. Chem.* **2009**, *30*, 2157.
- [87] R. Gautier, A. Bacle, M. L. Tiberti, P. F. Fuchs, S. Vanni, B. P. Antony, *Biophys. J.* **2018**, *115*, 436.
- [88] J. Jumper, R. Evans, A. Pritzel, T. Green, M. Figurnov, O. Ronneberger, K. Tunyasuvunakool, R. Bates, A. Židek, A. Potapenko, A. Bridgland, C. Meyer, S. A. A. Kohli, A. J. Ballard, A. Cowie, B. Romera-Paredes, S. Nikolov, R. Jain, J. Adler, T. Back, S. Petersen, D. Reiman, E. Clancy, M. Zielinski, M. Steinegger, M. Pacholska, T. Berghammer, S. Bodenstein, D. Silver, O. Vinyals, et al., *Nature* **2021**, *596*, 583.
- [89] M. Varadi, S. Anyango, M. Deshpande, S. Nair, C. Natassia, G. Yordanova, D. Yuan, O. Stroe, G. Wood, A. Laydon, A. Židek, T. Green, K. Tunyasuvunakool, S. Petersen, J. Jumper, E. Clancy, R. Green, A. Vora, M. Lutfi, M. Figurnov, A. Cowie, N. Hobbs, P. Kohli, G. Kleywegt, E. Birney, D. Hassabis, S. Velankar, *Nucl. Acids Res.* **2022**, *50*, D439.
- [90] P. J. A. Cock, T. Antao, J. T. Chang, B. A. Chapman, C. J. Cox, A. Dalke, I. Friedberg, T. Hamelryck, F. Kauff, B. Wilczynski, M. J. L. de Hoon, *Bioinformatics* **2009**, *25*, 1422.
- [91] T. A. Wassenaar, H. I. Ingólfsson, R. A. Böckmann, D. P. Tieleman, S. J. Marrink, *J. Chem. Theory Comput.* **2015**, *11*, 2144.
- [92] C. Kroon, P. A. A. Automate, P. (2020). *Aggregate, automate, assemble. [Thesis fully internal (DIV), University of Groningen]. University of Groningen*, **2020**, <https://doi.org/10.33612/diss.132963667>.
- [93] W. Kabsch, C. Sander, *Biopolymers* **1983**, *22*, 2577.
- [94] J. Kästner, W. Thiel, *J. Chem. Phys.* **2005**, *123*, 144104.
- [95] S.-W. Jin, D. Beis, T. Mitchell, J.-N. Chen, D. Y. R. Stainier, *Development* **2005**, *132*, 5199.